# Substrate Control for Large Area Continuous Films of Monolayer $MoS_2$ by Atmospheric Pressure Chemical Vapor Deposition

*Shanshan Wang[1], Merce Pacios[1], Harish Bhaskaran[1], Jamie H. Warner[1*]*

[1]Department of Materials, University of Oxford, Parks Road, Oxford, OX1 3PH, United Kingdom

*Jamie.warner@materials.ox.ac.uk;

**Abstract**

Growing monolayer $MoS_2$ films that are continuous with large domain sizes by chemical vapour deposition is one of the major challenges in 2D materials research at the moment. Here, we explore how atmospheric pressure CVD can be used to grow centimeter scale continuous films of monolayer $MoS_2$ films directly on Si substrates with an oxide layer whilst also obtaining large domain sizes exceeding 20 microns within the films. This is achieved by orientating the growth substrate in a vertical position to improve the uniformity of precursor feed-stock compared to horizontally orientated growth substrates. This leads to continuous films of monolayer $MoS_2$ over a significantly larger area without the need for low-pressure vacuum systems or volatile precursors. This provides important insights into novel approaches for maximizing domain sizes within $MoS_2$ films, with concomitant large area uniform coverage.

Recently, monolayer transition metal dichalcogenides (TMDs), such as molybdenum disulphide ($MoS_2$), have become complementary to the zero-bandgap graphene due to their direct band gaps ($E_g$ = 1.8 eV), and show promise in various nanoelectronics, optoelectronics and flexible devices.[1–6] Substantial efforts have been devoted to developing reliable and scalable approaches to achieve $MoS_2$ thin layers, including; exfoliation,[7,8] hydrothermal synthesis,[9,10] physical vapor deposition (PVD)[11,12] and chemical vapor deposition (CVD). CVD is one of the most promising methods of producing large-area and high quality continuous $MoS_2$ thin films to meet the demands of future scale-up fabrication of $MoS_2$ devices. Several different precursors have been used to synthesize $MoS_2$ in CVD, including the sulphurization of the pre-deposited Mo thin films,[13] the thermolysis of $(NH_4)_2MoS_4$[14], the sulphurization of $MoO_3$[15–19] or $MoCl_5$[20], and the reaction between $Mo(CO)_6$ and $(C_2H_5)_2S$[21]. However, the production of the continuous, large-scale, high quality $MoS_2$ monolayer films still remains a significant challenge, because of the difficulties from either the layer number control or the large-area continuity. There have been a few reports about the realization of large-scale growth of continuous monolayer $MoS_2$ films via the sulphurization to either $MoO_3$[22–24] or $MoCl_5$[20], or through a metal-organic CVD (MOCVD) technique with precursors of $Mo(CO)_6$ and $(C_2H_5)_2S$ [21]. However, all the reactions occurred under the low pressure, which increases the complexity of the method and requirements of the experimental equipment, and the MOCVD method suffers from using precursors with relatively high toxicity. In this study, we demonstrate a CVD synthesis strategy of continuous and high-quality monolayer $MoS_2$ films in the order of centimetres directly on a $SiO_2$/Si substrate under atmospheric pressure by controlling the growth substrate orientation relative to the mass flux of precursor.

## Results and Discussion

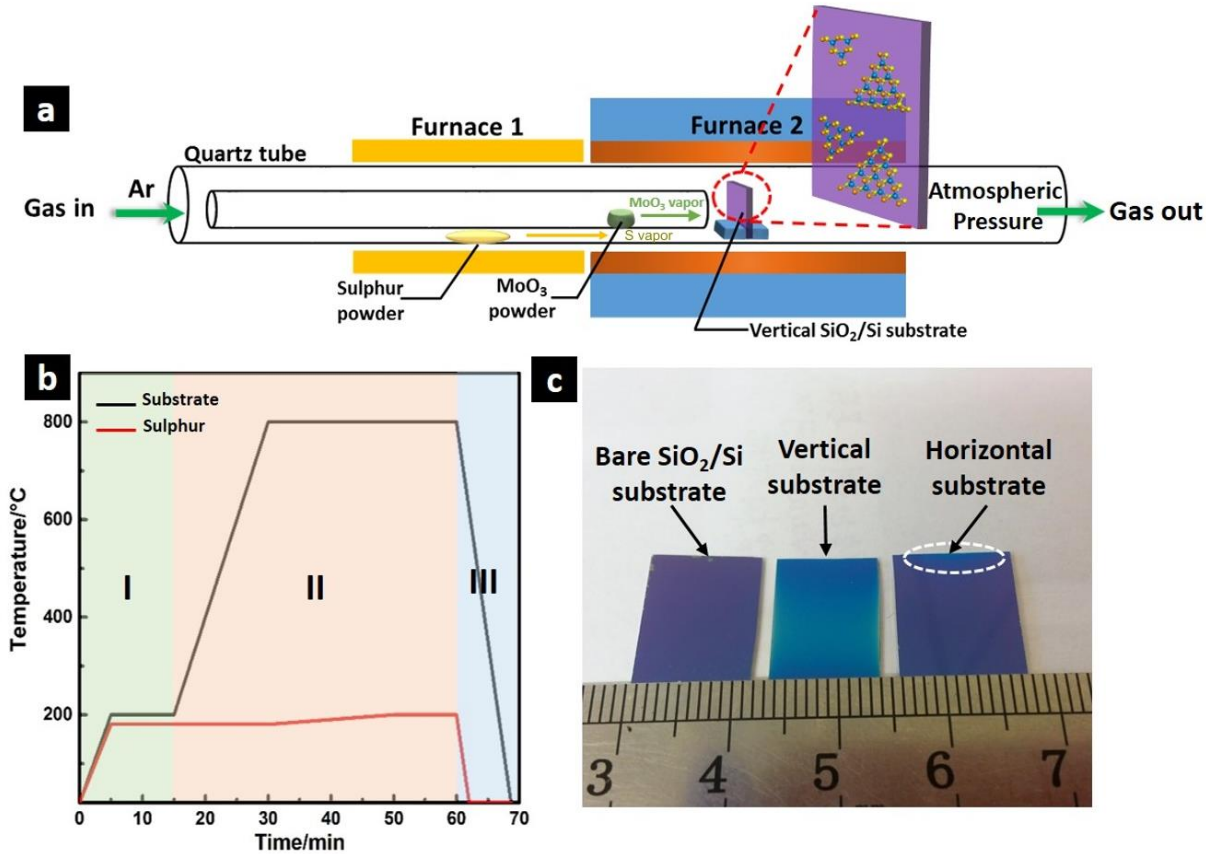


**Figure 1.** (a) Schematic illustration of the CVD synthesis setup of $MoS_2$. An zoom-in diagram is include to schematically illustrate the growth manner of $MoS_2$ crystals on the $SiO_2$ surface at the initial reaction stage, where individual monolayer $MoS_2$ domains randomly nucleate and grow, having contact with the substrate surface by (001) lattice plane. (b) Temperature programming process of $MoO_3$ and S precursors. (c) Optical images showing the contrast difference of bare $SiO_2$/Si substrate, the vertical substrate and the horizontal substrate after experiencing the same $MoS_2$ growth recipe.

As depicted in Figure 1a, $MoO_3$ (25 mg) and sulphur powder (600 mg) were used as precursors, loaded separately into two furnaces, 1 and 2, to provide independent temperature controls. A bare $SiO_2$/Si substrate (300 nm thick amorphous $SiO_2$ coated on the p-doped Si), was inserted into a homemade holder to keep it vertical, and was placed in furnace 2. This places the substrate surface to be perpendicular to the gas flow direction, decreasing the precursor concentration gradient on the $SiO_2$ and reduces the influence of the geometric effects from the gas flow by promoting the mass transport of precursors through the boundary layer above the substrate surface, which will be discussed in more detail afterwards. The sulphur precursor and the vertical substrate were both positioned in the central area of two furnaces, respectively, while the $MoO_3$ powder was upstream of the second furnace in order to produce a mild evaporation temperature for $MoO_3$. This enables better control over the nucleation density with flexibility of temperature adjustment by simply shifting the loading position. One of the $MoO_3$ locations for the best growth results was two centimetres away from the left open end of furnace 2. The reaction occurred under atmospheric pressure with argon used as carrier gas. We separated the two solid precursors by placing the $MoO_3$ into an inner quartz tube (diameter ~1 cm) inside the outer 1-inch tube with its inlet far exceeding the sulphur position. This avoids the gradual sulphurization of $MoO_3$ powder by sublimated sulphur, stabilizing the supply amount of both gaseous precursors to the reaction area around the substrate during the whole synthesis. The distance between the substrate surface and the outlet of the inner tube was 1.5 cm, which gives enough time for the even mixing of gaseous sulphur and $MoO_3$ and at the same time limits the formation of $MoS_2$ compounds in the gas phase that produce the three-dimensional $MoS_2$ flakes on the substrate. The growth can be divided into three sections: 1. Pre-introduction of S vapor to fill up the whole system by heating the sulphur powder up to 180°C for 15 minutes with an Ar flow rate of 150 sccm, creating a sulphur sufficient atmosphere (Figure 1b section I), 2. A main growth section with the typical temperatures for sulphur, $MoO_3$ and substrate to be 180-200°C, 300°C and 800°C, respectively, without changing the Ar flow rate (Figure 1b section II). 3. A fast cooling process with a 500 sccm Ar to quickly stop the reaction and accurately control the growth time.

To investigate the impact of the substrate loading on the final growth results, we did a direct comparison experiment by placing the substrate horizontally without changing any of the parameters. Figure 1c shows that compared with a bare $SiO_2$/Si chip the vertical substrate surface was uniformly covered by a $MoS_2$ film on the centimeter scale, showing green optical contrast different from the purple one from the bare substrate. For the horizontal substrate, the $MoS_2$ covered only a small top region on the substrate oriented to the gas inlet direction, which is marked by the dashed white ellipse, indicating a sharp precursor concentration decay on the substrate surface, when loading the $SiO_2$ surface to be parallel to the gas flow direction.

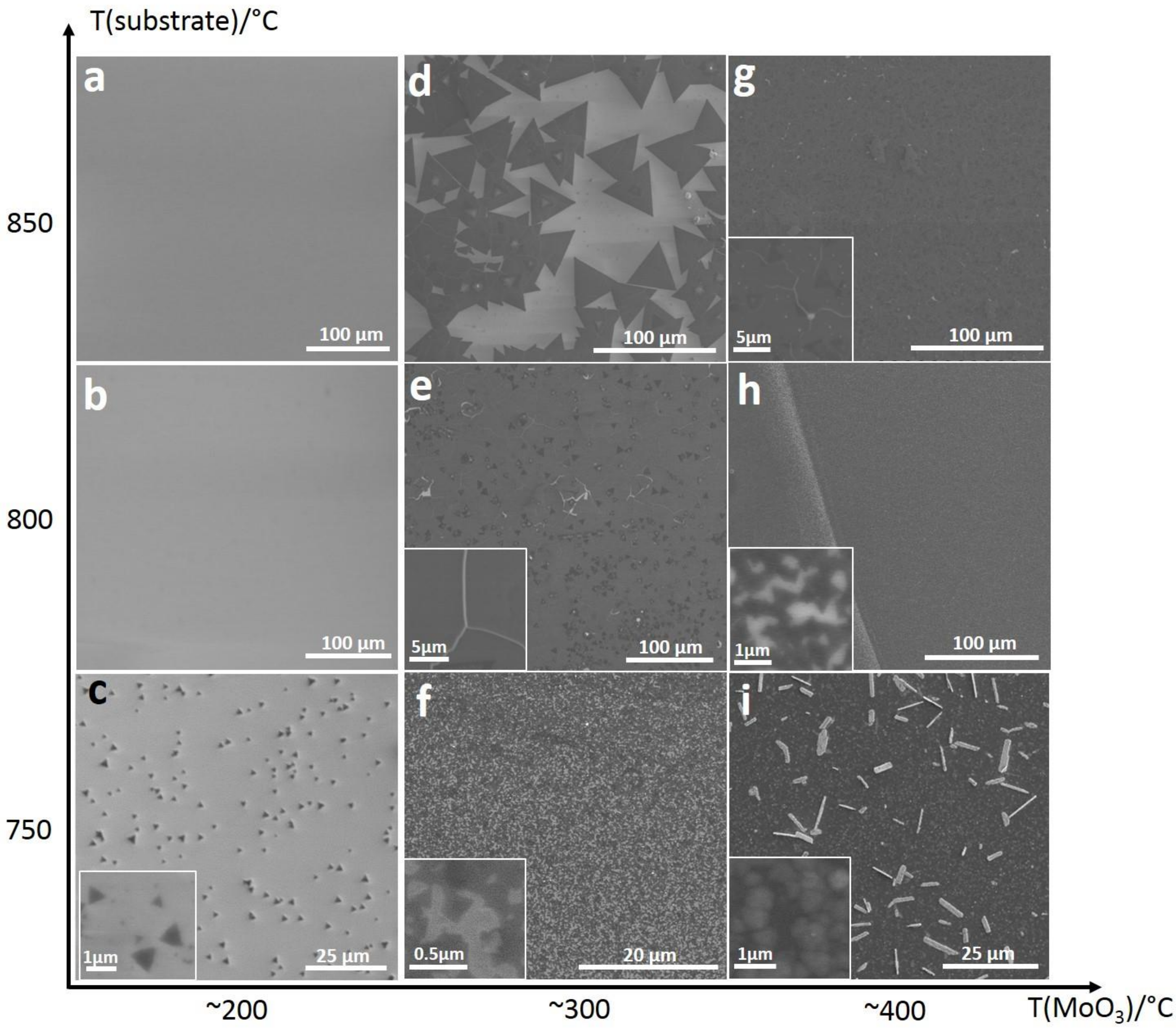


**Figure 2.** SEM images showing how the growth results depend on the parameters of the $MoO_3$ heating temperature and the substrate temperature (growth temperature), with magnified images as insets to highlight the detailed domain size and morphologies in panel c and e-i, respectively. Panel a and b show that there is nothing grown on the substrate under these conditions.

To gradually narrow down the range of growth parameters and optimize the $MoS_2$ film quality, several modifications were investigated, including the heating temperature of the precursor,

$MoO_3$, and the growth temperature (temperature for the substrate), which were found to be the key factors for synthesis. Figure 2 shows the $MoS_2$ growth dependence on these two parameters from a series of SEM images of the as-grown $MoS_2$ with their corresponding $MoO_3$ temperature and the growth temperature with magnified images as insets to highlight the detailed domain sizes and morphologies in panel c and e-i, respectively. In Figure 2c, 2f and 2i, for the growth temperature of 750 °C, when increasing the heating temperature of $MoO_3$ from 200°C to 400°C, the $MoS_2$ nucleation density goes up with a deterioration in the uniformity of the layer thickness, leading to island-like structures with smaller grain sizes. In contrast, when the $MoO_3$ temperature is fixed with a rise in the growth temperature, the nucleation density decreases with improved homogeneity in the layer thickness and higher crystallinity, evidenced by flatter surface morphology and the formation of larger triangular-shaped monolayer domains (Figure 2f, 2e and 2d). The reason for such a growth mode transition is attributed to the change of the mean free path of $MoS_2$ precursor elements on the substrate surface, which is influenced by both the $MoO_3$ heating temperature and the growth temperature. With higher $MoO_3$ temperature, the supply of gaseous $MoO_3$ will be more sufficient, leading to a larger amount of $MoS_2$ species on the substrate surface, initiating new nuclei instead of attaching to the existing nuclei already formed. That is why the nucleation density increases with smaller grains grown when the $MoO_3$ temperature rises. In contrast, with higher growth temperature, the mean free diffusion path of $MoS_2$ precursor molecules could be longer due to a reduction of the amount of $MoS_2$ species absorbed on the substrate surface, leading to attachment to preformed nuclei and expanding the crystal size rather than forming new nuclei. This results in decreasing nucleation density with larger domains produced as the growth temperature increases. In addition, the increased growth temperature is expected to increase the crystallinity of $MoS_2$, evidenced by an improvement on the domain shape faceting. It is also worth noting that the best growth recipe is a combination of both the temperatures of the $MoO_3$ and the substrate, respectively. It is possible to obtain similar mean free diffusion paths of $MoS_2$ precursor species for different combinations of these temperatures, and thus obtain uniform full coverage of monolayer $MoS_2$ for two different parameters (Figure 2e and 2g).

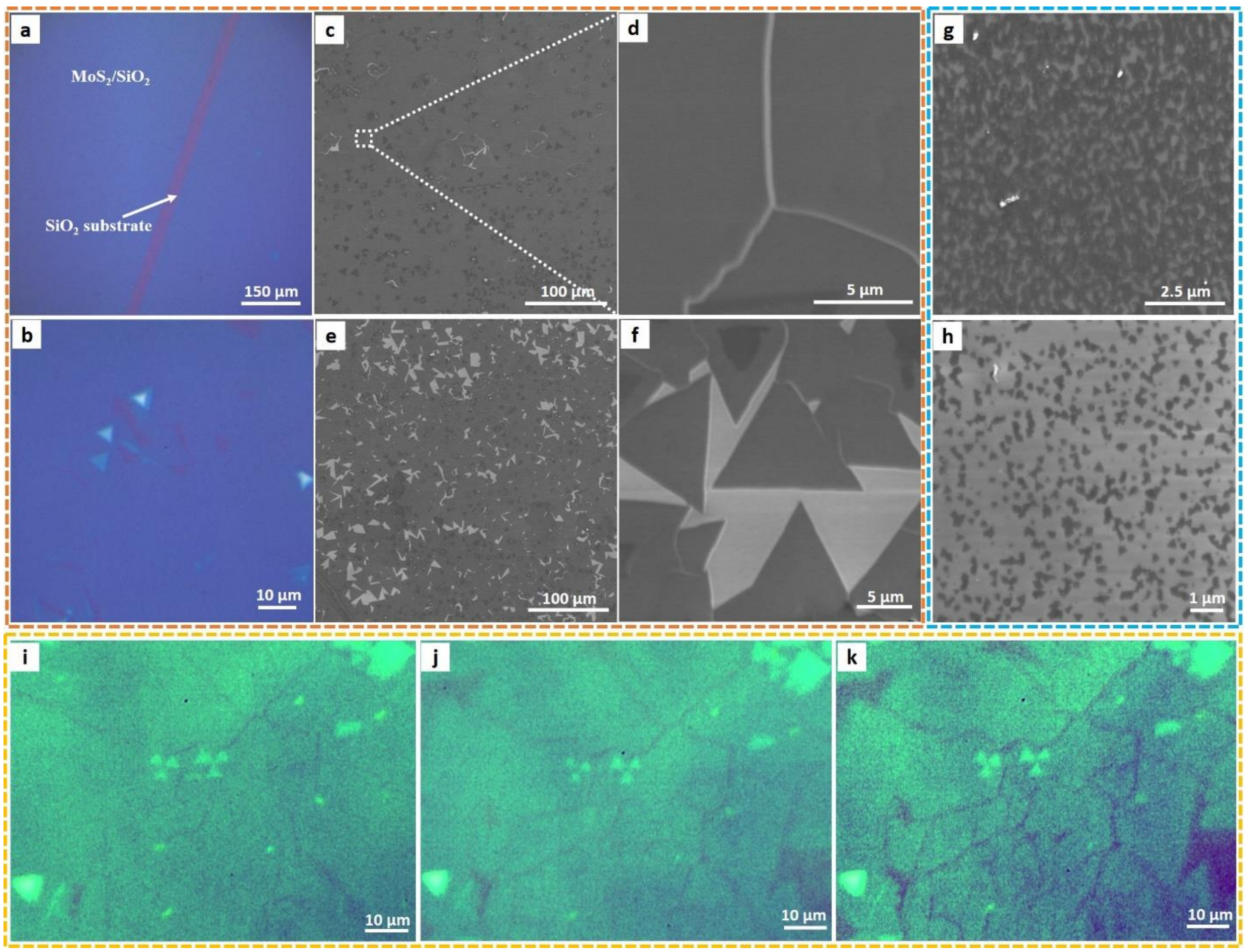


**Figure 3.** (a-b) Low-magnification and high-magnification optical images of an as-grown continuous $MoS_2$ film, respectively. (c) Low-magnification SEM image of the $MoS_2$ continuous film, where $MoS_2$ domains are fully merged. (d) Higher magnification SEM image of the area marked in the white dashed box in panel c, showing the uniform-grown $MoS_2$ film with micro-cracks or wrinkles potentially induced by the fast-cooling process. (e) Low-magnification SEM image of a growth area near the substrate boundary, where triangular $MoS_2$ domains nearly merge into a continuous film. (f). High-magnification SEM image of the same area as panel e, showing the coalescence of triangular $MoS_2$ domains with a side length of 10-15µm. (g-h) SEM images of $MoS_2$ in the top region of the horizontal

substrate using the same recipe. (i-k) Optical images of the $MoS_2$ continuous thin film before (i) and after the oxidation treatment in the air for 70 min (j) and 100 min (k), respectively, at a temperature of 300 °C to reveal the grain boundaries.

Figure 3a shows a low-magnification optical image of a typical $MoS_2$ film grown on the $SiO_2$/Si substrate with an intentional scratch introduced to show the optical contrast difference between the $MoS_2$ film and the bare substrate. Figure 3b shows more detailed information, indicating that most of the area is uniformly covered by a continuous monolayer $MoS_2$ film, with only a very small portion of multilayer regions with brighter optical contrast (the proof of the $MoS_2$ thickness uniformity will be given by the following PL and Raman characterization in Figure 4). The scanning electron microscopy (SEM) images in Figure 3c and 3d are consistent with the optical images, confirming the large-area and continuous growth of monolayer $MoS_2$ films, with the presence of micro-cracks or winkles potentially induced by the fast-cooling step because of the thermal expansion coefficient difference between the monolayer $MoS_2$ and $SiO_2$. When choosing an area close to the substrate boundary, where the substrate surface is not fully covered by $MoS_2$, the continuous films are formed by the gradual merger of isolated monolayer triangular $MoS_2$ domains with sizes of 10-15 μm (Figure 3e and f). To better evaluate the grain size of the $MoS_2$ membrane, we carried out an oxidation treatment at a temperature of 300°C in air, which has been previously shown to reveal the grain boundaries in TMD films under an optical microscope.[22,25] As shown in Figure 3i to 3k, the grain boundaries were gradually etched out after oxidizing for 70 and 100 min, respectively, and the crystal size was confirmed to be around 10 to 20 μm, which is larger than that of the $MoS_2$ monolayer films obtained by other low pressure CVD techniques,[21,22] and is in agreement with the observations in Figure 3e and f. We have also characterized the growth results when loading the $SiO_2$/Si substrates horizontally. As shown in Figure 3g, large amounts of nanometer-sized, isolated and irregular-shaped $MoS_2$ domains were densely distributed in the top region of the substrate. When taking the SEM image ~300μm away from the location in Figure 3g to the downstream of the substrate, the nucleation density of the $MoS_2$ domains dramatically decreases, Figure 3h, indicating a sharp precursor concentration gradient on the $SiO_2$ surface, which hinders the production of large-area and homogeneous $MoS_2$ films.

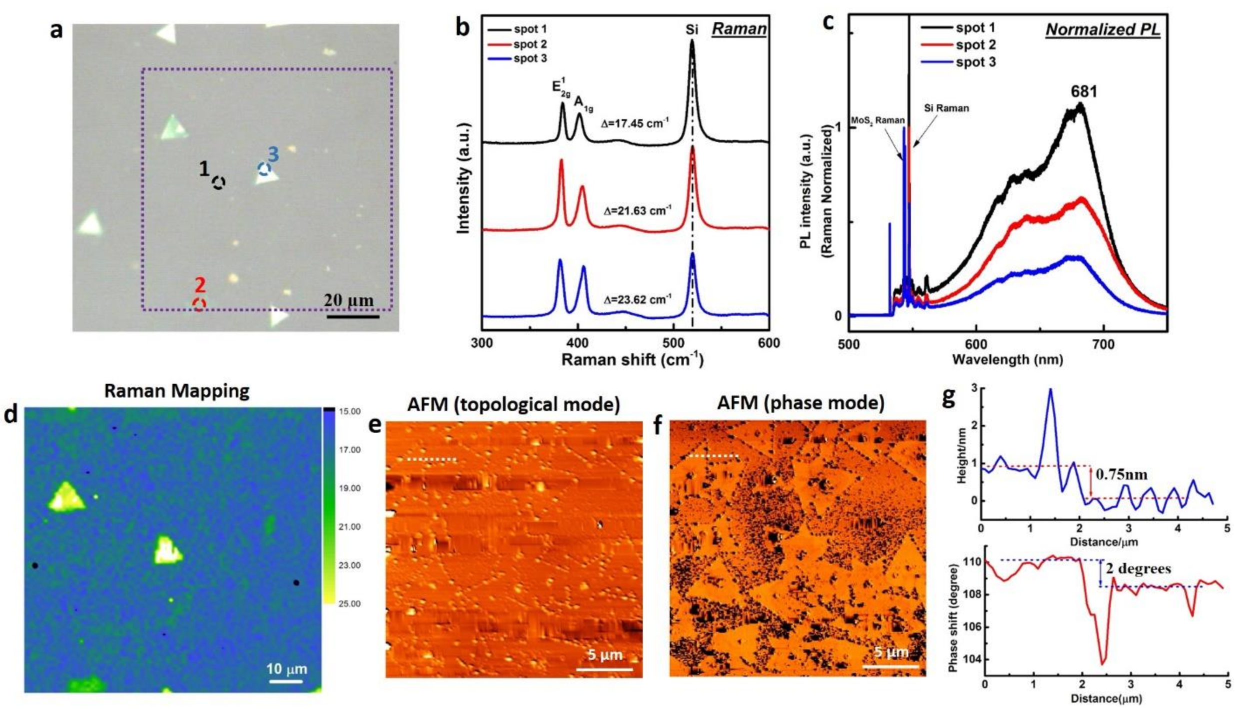


**Figure 4.** (a) Optical images of the $MoS_2$ continuous film, showing monolayers in most areas with only a small percentage of multi-layer regions. (b) Raman and normalized photoluminescence spectrum from three marked spots numbered by 1,2 and 3, respectively, with corresponding coloured circles in (a). (d) Raman maps of the $MoS_2$ film in the square marked by a dashed purple outline in (a), plotting the 2D spatial variation of the magnitude of the frequency difference between $A_{1g}$ and $E^1_{2g}$. Laser excitation of 532 nm was used. (e-f) AFM images in the topological and phase mode, respectively, of a nearly fully-merged $MoS_2$ growth region. (g) Height and phase profiles taken across the same $MoS_2$ edge marked by dotted white lines in panel e and f, respectively.

We used Raman and photoluminescence (PL) spectroscopy, as well as atomic force microscopy (AFM) to evaluate the thickness, quality and uniformity of the as-grown $MoS_2$ films.

Figure 4a-c provides the optical image together with the Raman and PL spectra from the spots marked with the corresponding coloured circles shown in panel a. There are two characteristic Raman peaks for $MoS_2$, $E^1_{2g}$ and $A_{1g}$, which represent the in-plane vibration of Mo and S atoms and the out-of-plane vibration of S atoms, respectively.[26] The frequency difference between these two peaks is dependent on the layer number, which is used to determine the $MoS_2$ thickness.[27,28] The fitting results shows that $MoS_2$ from the black spot has the $E^1_{2g}$ and $A_{1g}$ modes located at 384.1 and 401.6 $cm^{-1}$, respectively, with a peak spacing of ~17.5 $cm^{-1}$, which is consistent with the exfoliated monolayer $MoS_2$.[29] The full width of half maximum (FWHM) of $E^1_{2g}$ is ~4.6 $cm^{-1}$, suggesting good crystallinity of the CVD-grown $MoS_2$.[20] The Raman spectra of $MoS_2$ with a lighter green contrast (red spot) and a bright white contrast (blue spot) show an increased frequency difference ($\Delta$) between $E^1_{2g}$ and $A_{1g}$ peak, having $\Delta$ to be ~ 21.6 and ~23.6 $cm^{-1}$, respectively, indicating thickness of bilayer and multilayers (>3 layers). We have also characterized the PL spectra from the same three spots, and normalized the $MoS_2$ PL signal by its Raman intensity to better reveal the PL quantum efficiency dependence on the $MoS_2$ layer number, because such a normalized PL can cancel out the influence from many external effects, such as laser excitation intensity, quantity of materials, and local electric field factors.[26] As shown in Figure 4c, the PL spectra from monolayer $MoS_2$ (black spot) exhibits the highest PL intensity, with two pronounced emission peaks at ~681 and ~627nm, respectively, corresponding to the $A_1$ and $B_1$ direct excitonic transitions. The emission intensity obviously reduces for bilayer and multilayer regions, due to the bandgap shifting from direct to indirect transitions with the increase of $MoS_2$ thickness. 2D Raman mapping was performed over an area of 100 μm × 100 μm in the continuous $MoS_2$ film (marked by the dashed purple square in panel a) by plotting the spatial variation of the magnitude of the frequency difference between $A_{1g}$ and $E^1_{2g}$ peaks (Figure 4d). The thickness distribution correlates well to the contrast on the optical image in panel a, having more than 90% of the area with a frequency difference to be less than ~19 $cm^{-1}$ with a small fraction of bilayer or multilayer flakes, which confirms large area uniform monolayer $MoS_2$ was grown on $SiO_2$. The AFM measurements in the topological mode of an almost fully-merged region (Figure 4e, the 'almost fully-merged region' means an area densely covered by triangular $MoS_2$ domains, which are close to coalesce into continues films, being similar as the region shown in Figure 3e and f.) with the corresponding height profile evaluating the layer thickness across the area marked by a white dotted line in Figure 4e (the height curve in the upper part of Figure 4g) were provided as a more direct way to determine the $MoS_2$ layer number and uniformity. A thickness of 0.75 nm is obtained, in agreement with the $MoS_2$ monolayer thickness.[20,23,30] Since the thickness of monolayer $MoS_2$ is quite small, to better distinguish the coverage region of $MoS_2$ films from the bare $SiO_2$/Si substrate, phase mode mapping is shown in Figure 4f, where the visibility of partially merged $MoS_2$ monolayers increases because of the elasticity difference between $MoS_2$ and $SiO_2$.  The phase profile in the lower part of Figure 4g shows that the phase change of the AFM tip vibration when moving from the surface of monolayer $MoS_2$ to $SiO_2$ is ~2 degrees.

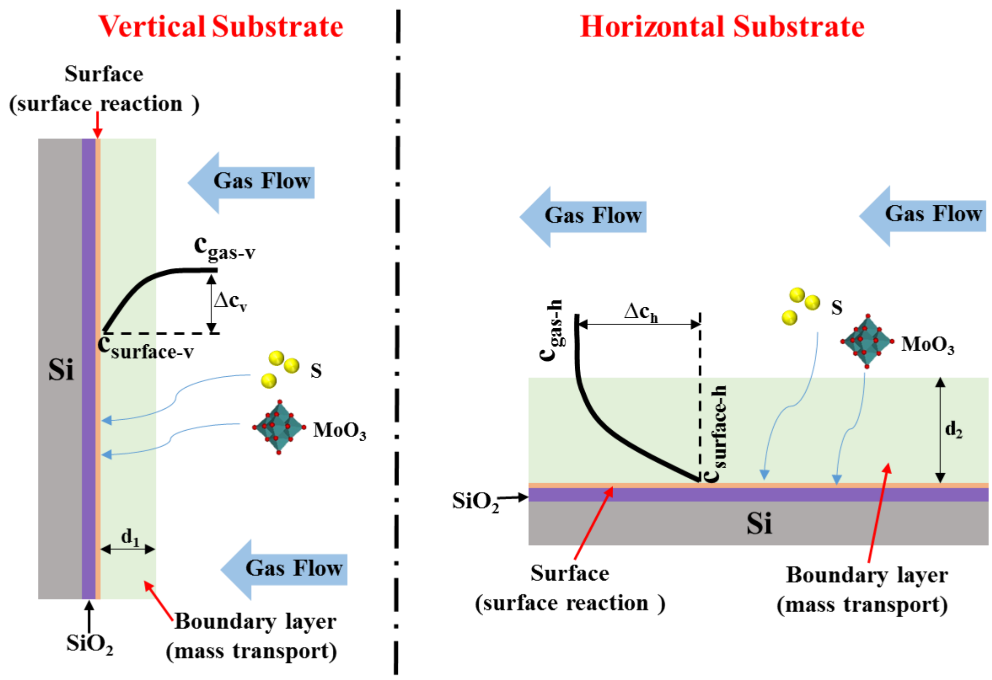


**Figure 5.** A schematic illustration showing how the loading of the substrate influences the final rate-limiting step of the whole $MoS_2$ growth procedure. Since the vertically-loaded substrate reduces the diffusion energy barrier for the gaseous precursors to reach the substrate surface, a thinner boundary layer forms compared to the horizontal loaded substrate under the same experimental parameters ($c_{gas-v} = c_{gas-h}$, $c_{gas-v}$ and $c_{gas-h}$ represent the precursor concentrations in the bulk gas flow, when putting the substrate in a vertical or horizontal orientation, respectively.). The precursor concentration on the vertical substrate surface is higher than that on the horizontal one ($c_{surface-v} > c_{surface-h}$, $c_{surface-v}$ and $c_{surface-h}$ represent the precursor concentration on the substrate surface of a vertical or horizontal substrate, respectively). This contributes to the increase of the surface reaction rate, and could switch the rate-limiting step of the growth from the mass transport process to the surface reaction process, which is a significant requirements to realize the large-area uniform $MoS_2$ film production.

We now discuss the influence of the substrate orientation on the $MoS_2$ growth from a kinetic growth model perspective (Figure 5). Briefly, the two-dimensional $MoS_2$ growth can be divided into two procedures: (1) the mass transport of precursors through the boundary layer to reach the substrate surface, and (2) the reaction chemistry for precursors on the substrate surface, primarily involving the absorption/desorption and migration of precursor molecules on the surface and the reactions involving the Mo-precursor and sulphur. In the CVD growth of graphene under atmospheric conditions at a high temperature, mass transport is typically the rate-limiting step.[31] For mass transport processes, factors such as the geometry of the precursor gas flow can easily impact the thickness of the boundary layer and cause variation in the amount of precursor species on the surface. This will eventually result in thickness non-uniformity of the as-grown materials. For the synthesis of 2D $MoS_2$, using two solid-state precursors, $MoO_3$ and sulphur, the way they physically mix will also be important, and is more challenging to achieve uniformly mixed precursors than the case of pure gaseous precursors used in graphene CVD. Loading the substrate vertically with its surface perpendicular to the gas flow direction is a simple way to achieve uniform precursor concentrations and mixing, while also decreasing the thickness of the boundary layer, since it reduces the diffusion energy barrier for the gaseous precursors to reach the substrate surface, as shown in the left panel of Figure 5. On the contrary, for the horizontal substrate under the same growth conditions, the boundary layer is thicker than the vertical substrate, which leads to a sharp precursor concentration reduction when going through the boundary layer, hindering the amount of precursor species on the substrate surface and limiting the growth of 2D $MoS_2$. The $MoS_2$ grown on the top edge of the horizontal substrate could be attributed to the flow disturbance when the gas flow initially meets the edge of the substrate, which reduces the boundary layer thickness around that region. However, as the migration distance for precursor molecules on the surface is very limited, the surface precursor concentration will decay sharply along the gas flow direction. This helps explain why the $MoS_2$ coverage percentage dramatically decreases when moving further downstream along the horizontal substrate. In brief, the most prominent difference between the vertical and horizontal substrate is that the first loading manner can achieve a higher precursor concentration with spatial uniformity on the surface under the same growth condition, which contributes to the increase of the surface reaction rate, and could switch the rate-limiting step of the growth from the mass transport process to the surface reaction process. This effectively reduces the geometric effect from the flow of two types of gaseous precursors and is a significant requirement to realize the large-area uniform $MoS_2$ film production.

## Conclusion

In conclusion, we report a simple approach for growing centimeter-scale, high quality and predominantly monolayer $MoS_2$ films with large domain sizes, directly on the $SiO_2$/Si substrate using vertically orientated substrates in CVD at atmospheric pressure. The film microstructure, thickness, homogeneity and quality were characterized by optical microscopy, SEM, Raman spectra, AFM and PL spectra and confirm the quality of the material. This approach has potential to scale up further by increasing the diameter of the reaction quartz tube in the furnace to reach the 4 inch size. By avoiding the use of highly toxic metal organic precursors, our approach has the potential for industrial compatibility in scale up and easily meets safety requirements for commercial implementation. These results show how sensitive the growth of monolayer materials are to minor variations in the CVD geometry and that drastic improvements can be easily achieved by simple optimizations.

## Experimental Methods

The $MoS_2$ film was grown on a $SiO_2$ (300 nm)/p++Si substrate (University Wafer), which is sonicated in the acetone and 2-propanol solution sequentially, followed by an oxygen plasma treatment. The growth was carried out in a CVD system using 25 mg of $MoO_3$ powder (≥99.5%, Sigma-Aldrich) and 600 mg of S (≥99.5%, Sigma-Aldrich) as the precursor with argon (Ar) as carrier gas under atmospheric pressure. The S powder was placed at the central area of Furnace 1 in the outer 1-inch quartz tube, while the $MoO_3$ was loaded separately at the upstream of Furnace 2, in an inner quartz tube having a smaller diameter of 1 cm. The distance between the $MoO_3$ and the left open of Furnace 2 was designed to be ~2 cm, and the vertical substrate was placed in the center of the second furnace. The growth system was first flushed with 500 sccm of Ar gas for 30 min, followed by a pre-introduction of S vapor by heating the S powder up to ~180°C for 15 min under an Ar flow rate of 150 sccm. Furnace 2 was maintained at 200°C at the same time to avoid any deposition of the solid S on the substrate surface. This ensured the reaction to occur under an S sufficient atmosphere and could effectively control the $MoS_2$ nucleation density at the initial stage. Then, Furnace 2 was heated up at a rate of 40°C/min to 800°C, while $MoO_3$ powder reached an approximate maximum temperature of 300°C. The S powder temperature was programmed to increase from 180 to 200°C at a rate of 1°C/min as soon as the Furnace 2 reached 800°C. Such a temperature enhancement is to complement the consumption of the S powder amount to maintain the S rich growth environment. The reaction was conducted under the temperature of 800°C for 30 min with 500 sccm Ar. After it, a fast cooling process was applied to quickly stop the growth.

**Characterization**

The morphology of the continuous $MoS_2$ monolayer films was characterized using a scanning electron microscope (Hitachi-4300) under an accelerating voltage of 3.0 kV. Raman spectroscopy and photoluminescence were conducted using a JY Horiba LabRAM ARAMIS imaging confocal Raman microscope. The excitation light is a 532 nm laser with an estimated laser spot size of 1 µm. For the measurement of Raman mapping, the acquisition time is 0.1 seconds for each spot with a step size of 1µm. The film thickness and surface topology were analyzed by an atomic force microscope (Asylum Research MFP-3D) in AC mode with a silicon AC-160TS cantilever (Olympus, spring constant of ~42 N/m and resonant frequency of ~300 kHz).

## Acknowledgements

J.H.W. thanks the Royal Society for support. S. W. acknowledges financial support from the China Scholarship Council.

## Reference

(1) Radisavljevic, B.; Radenovic, A; Brivio, J.; Giacometti, V.; Kis, A. Single-Layer $MoS_2$ Transistors. *Nat. Nanotechnol.* **2011**, *6*, 147–150.

(2) Wang, Q. H.; Kalantar-Zadeh, K.; Kis, A.; Coleman, J. N.; Strano, M. S. Electronics and Optoelectronics of Two-Dimensional Transition Metal Dichalcogenides. *Nat. Nanotechnol.* **2012**, *7*, 699–712.

(3) Amani, M.; Chin, M. L.; Birdwell, A. G.; O'Regan, T. P.; Najmaei, S.; Liu, Z.; Ajayan, P. M.; Lou, J.; Dubey, M. Electrical Performance of Monolayer $MoS_2$ Field-Effect Transistors Prepared by Chemical Vapor Deposition. *Appl. Phys. Lett.* **2013**, *102*, 193107.

(4) Li, H.; Yin, Z.; He, Q.; Li, H.; Huang, X.; Lu, G.; Fam, D. W. H.; Tok, A. I. Y.; Zhang, Q.; Zhang, H. Fabrication of Single- and Multilayer $MoS_2$ Film-Based Field-Effect Transistors for Sensing NO at Room Temperature. *Small* **2012**, *8*, 63–67.

(5) Ganatra, R.; Zhang, Q. Few-Layer MoS2: A Promising Layered Semiconductor. *ACS Nano* **2014**, *8*, 4074–4099.

(6) Balendhran, S.; Walia, S.; Nili, H.; Ou, J. Z.; Zhuiykov, S.; Kaner, R. B.; Sriram, S.; Bhaskaran, M.; Kalantar-zadeh, K. Two-Dimensional Molybdenum Trioxide and Dichalcogenides. *Adv. Funct. Mater.* **2013**, *23*, 3952–3970.

(7) Zhou, K.-G.; Mao, N.-N.; Wang, H.-X.; Peng, Y.; Zhang, H.-L. A Mixed-Solvent Strategy for Efficient Exfoliation of Inorganic Graphene Analogues. *Angew. Chem. Int. Ed. Engl.* **2011**, *50*, 10839–10842.

(8) Zeng, Z.; Yin, Z.; Huang, X.; Li, H.; He, Q.; Lu, G.; Boey, F.; Zhang, H. Single-Layer Semiconducting Nanosheets: High-Yield Preparation and Device Fabrication. *Angew. Chem. Int. Ed. Engl.* **2011**, *50*, 11093–11097.

(9) Dunne, P. W.; Munn, A. S.; Starkey, C. L.; Lester, E. H. The Sequential Continuous-Flow

Hydrothermal Synthesis of Molybdenum Disulphide. *Chem. Commun.* **2015**, *51*, 4048–4050.

(10) Rao, C. N. R.; Nag, A. Inorganic Analogues of Graphene. *Eur. J. Inorg. Chem.* **2010**, *2010*, 4244–4250.

(11) Gong, C.; Huang, C.; Miller, J.; Cheng, L.; Hao, Y.; Cobden, D.; Kim, J.; Ruoff, R. S.; Wallace, R. M.; Cho, K.; et.al. Metal Contacts on Physical Vapor Deposited Monolayer $MoS_2$. *ACS Nano* **2013**, *7*, 11350–11357.

(12) Wu, S.; Huang, C.; Aivazian, G.; Ross, J. S.; Cobden, D. H.; Xu, X. Vapor–Solid Growth of High Optical Quality $MoS_2$ Monolayers with Near-Unity Valley Polarization. *ACS Nano* **2013**, *7*, 2768–2772.

(13) Zhan, Y.; Liu, Z.; Najmaei, S.; Ajayan, P. M.; Lou, J. Large-Area Vapor-Phase Growth and Characterization of $MoS_2$ Atomic Layers on a $SiO_2$ Substrate. *Small* **2012**, *8*, 966–971.

(14) Liu, K.-K.; Zhang, W.; Lee, Y.-H.; Lin, Y.-C.; Chang, M.-T.; Su, C.-Y.; Chang, C.-S.; Li, H.; Shi, Y.; Zhang, H.; et al. Growth of Large-Area and Highly Crystalline $MoS_2$ Thin Layers on Insulating Substrates. *Nano Lett.* **2012**, *12*, 1538–1544.

(15) van der Zande, A. M.; Huang, P. Y.; Chenet, D. A; Berkelbach, T. C.; You, Y.; Lee, G.-H.; Heinz, T. F.; Reichman, D. R.; Muller, D. A; Hone, J. C. Grains and Grain Boundaries in Highly Crystalline Monolayer Molybdenum Disulphide. *Nat. Mater.* **2013**, *12*, 554–561.

(16) Najmaei, S.; Liu, Z.; Zhou, W.; Zou, X.; Shi, G.; Lei, S.; Yakobson, B. I.; Idrobo, J.-C.; Ajayan, P. M.; Lou, J. Vapour Phase Growth and Grain Boundary Structure of Molybdenum Disulphide Atomic Layers. *Nat. Mater.* **2013**, *12*, 754-759.

(17) Wang, X.; Feng, H.; Wu, Y.; Jiao, L. Controlled Synthesis of Highly Crystalline $MoS_2$ Flakes by Chemical Vapor Deposition. *J. Am. Chem. Soc.* **2013**, *135*, 5304–5307.

(18) Ling, X.; Lee, Y.-H.; Lin, Y.; Fang, W.; Yu, L.; Dresselhaus, M. S.; Kong, J. Role of the Seeding Promoter in $MoS_2$ Growth by Chemical Vapor Deposition . *Nano Lett*. **2014**, *14*, 464–472.

(19) Wang, S.; Rong, Y.; Fan, Y.; Pacios, M.; Bhaskaran, H.; He, K.; Warner, J. H. Shape

Evolution of Monolayer $MoS_2$ Crystals Grown by Chemical Vapor Deposition. *Chem. Mater.* **2014**, *26*, 6371–6379.

(20) Yu, Y.; Li, C.; Liu, Y.; Su, L.; Zhang, Y.; Cao, L. Controlled Scalable Synthesis of Uniform, High-Quality Monolayer and Few-layer $MoS_2$ Films. *Sci. Rep.* **2013**, *3*, 1866.

(21) Kang, K.; Xie, S.; Huang, L.; Han, Y.; Huang, P. Y.; Mak, K. F.; Kim, C.-J.; Muller, D.; Park, J. High-Mobility Three-Atom-Thick Semiconducting Films with Wafer-Scale Homogeneity. *Nature* **2015**, *520*, 656–660.

(22) Zhang, J.; Yu, H.; Chen, W.; Tian, X.; Liu, D.; Cheng, M.; Xie, G.; Yang, W.; Yang, R.; Bai, X.; et al. Scalable Growth of High-Quality Polycrystalline $MoS_2$ Monolayers on SiO2 with Tunable Grain Sizes. *ACS Nano* **2014**, *8*, 6024–6030.

(23) Senthilkumar, V.; Tam, L. C.; Kim, Y. S.; Sim, Y.; Seong, M.-J.; Jang, J. I. Direct Vapor Phase Growth Process and Robust Photoluminescence Properties of Large Area $MoS_2$ Layers. *Nano Res.* **2014**, *7*, 1759–1768.

(24) Jeon, J.; Jang, S. K.; Jeon, S. M.; Yoo, G.; Jang, Y. H.; Park, J.-H.; Lee, S. Layer-Controlled CVD Growth of Large-Area Two-Dimensional $MoS_2$ Films. *Nanoscale* **2015**, *7*, 1688–1695.

(25) Rong, Y.; He, K.; Pacios, M.; Robertson, A. W.; Bhaskaran, H.; Warner. J. H. Controlled Preferential Oxidation of Grain Boundaries in Monolayer Tungsten Disulfide for Direct Optical Imaging. **2015**, *ACS Nano* **2015**, *9*, 3695–3703.

(26) Splendiani, A.; Sun, L.; Zhang, Y.; Li, T.; Kim, J.; Chim, C.-Y.; Galli, G.; Wang, F. Emerging Photoluminescence in Monolayer $MoS_2$. *Nano Lett.* **2010**, *10*, 1271–1275.

(27) Lee, Y.-H.; Zhang, X.-Q.; Zhang, W.; Chang, M.-T.; Lin, C.-T.; Chang, K.-D.; Yu, Y.-C.; Wang, J. T.-W.; Chang, C.-S.; Li, L.-J.; Lin, T.-W. Synthesis of Large-Area $MoS_2$ Atomic Layers with Chemical Vapor Deposition. *Adv. Mater.* **2012**, *24*, 2320–2325.

(28) Tonndorf, P.; Schmidt, R.; Böttger, P.; Zhang, X.; Börner, J.; Liebig, A.; Albrecht, M.; Kloc, C.; Gordan, O.; Zahn, D. R. T.; et al. Photoluminescence Emission and Raman Response of Monolayer $MoS_2$, $MoSe_2$, and $WSe_2$. *Opt. Express* **2013**, *21*, 4908–4916.

(29) Li, S.-L.; Miyazaki, H.; Song, H.; Kuramochi, H.; Nakaharai, S.; Tsukagoshi, K. Quantitative Raman Spectrum and Reliable Thickness Identification for Atomic Layers on

Insulating Substrates. *ACS Nano* **2012**, *6*, 7381–7388.

(30) Lee, Y.-H.; Yu, L.; Wang, H.; Fang, W.; Ling, X.; Shi, Y.; Lin, C.-T.; Huang, J.-K.; Chang, M.-T.; Chang, C.-S.; et al. Synthesis and Transfer of Single-Layer Transition Metal Disulfides on Diverse Surfaces. *Nano Lett.* **2013**, *13*, 1852–1857.

(31) Bhaviripudi, S.; Jia, X.; Dresselhaus, M. S.; Kong, J. Role of Kinetic Factors in Chemical Vapor Deposition Synthesis of Uniform Large Area Graphene Using Copper Catalyst. *Nano Lett.* **2010**, *10*, 4128–4133.

**TOC graphic**